

# Unraveling the magnetic ground-state in alkali-metal lanthanide oxide $\text{Na}_2\text{PrO}_3$

Ifeanyi John Onuorah,<sup>1</sup> Jonathan Frassinetti,<sup>2</sup> Qiaochu Wang,<sup>3</sup> Muhammad Maikudi Isah,<sup>2</sup> Pietro Bonfà,<sup>1</sup> Jeffrey G. Rau,<sup>4</sup> J. A. Rodriguez-Rivera,<sup>5,6</sup> A. I. Kolesnikov,<sup>7</sup> Vesna F. Mitrović,<sup>3</sup> Samuele Sanna,<sup>2</sup> and Kemp W. Plumb<sup>3</sup>

<sup>1</sup>*Dipartimento di Scienze Matematiche, Fisiche e Informatiche, Università di Parma, I-43124 Parma, Italy*

<sup>2</sup>*Dipartimento di Fisica e Astronomia "A. Righi", Università di Bologna, I-40127 Bologna, Italy*

<sup>3</sup>*Department of Physics, Brown University, Providence, Rhode Island 02912, USA*

<sup>4</sup>*Department of Physics, University of Windsor, Windsor, Ontario, Canada N9B 3P4*

<sup>5</sup>*NIST Center for Neutron Research, National Institute of Standards and Technology, Gaithersburg, MD 20899, USA*

<sup>6</sup>*Department of Materials Science and Engineering, University of Maryland, College Park, MD 20742, USA*

<sup>7</sup>*Neutron Scattering Division, Oak Ridge National Laboratory, Oak Ridge, Tennessee 37831, USA*

(Dated: July 19, 2024)

A comprehensive set of muon spin spectroscopy and neutron scattering measurements supported by ab-initio and model Hamiltonian simulations have been used to investigate the magnetic ground state of  $\text{Na}_2\text{PrO}_3$ .  $\mu\text{SR}$  reveals a Néel antiferromagnetic order below  $T_N \sim 4.9$  K, with a small static magnetic moment  $m_{\text{static}} \leq 0.22 \mu_B/\text{Pr}$  collinearly aligned along the  $c$ -axis. Inelastic neutron measurements reveal the full spectrum of crystal field excitations and confirm that the  $\text{Pr}^{4+}$  ground state wave function deviates significantly from the  $\Gamma_7$  limit that is relevant to the Kitaev model. Single and two magnon excitations are observed in the ordered state below  $T_N = 4.6$  K and are well described by non-linear spin wave theory from the Néel state using a magnetic Hamiltonian with Heisenberg exchange  $J = 1$  meV and symmetric anisotropic exchange  $\Gamma/J = 0.1$ , corresponding to an XY model. Intense two magnon excitations are accounted for by  $g$ -factor anisotropy  $g_z/g_{\pm} = 1.29$ . A fluctuating moment  $\delta m^2 = 0.57(22) \mu_B^2/\text{Pr}$  extracted from the energy and momentum integrated inelastic neutron signal is reduced from expectations for a local  $J = 1/2$  moment with average  $g$ -factor  $g_{\text{avg}} \approx 1.1$ . Together, the results demonstrate that the small moment in  $\text{Na}_2\text{PrO}_3$  arises from crystal field and covalency effects and the material does not exhibit significant quantum fluctuations.

## I. INTRODUCTION

Material realizations of Heisenberg-Kitaev models hold significant contemporary interest because of their potential to harbor quantum spin liquids in higher than one-dimensional lattice geometries [1–3]. The Kitaev model is characterized by quantum frustration arising from bond-dependent anisotropic Kitaev interactions between  $J_{\text{eff}} = 1/2$  Kramer's doublets spin-orbit entangled local magnetic moments [1, 4]. In practice, the generic Hamiltonian for a realistic Kitaev material contains Heisenberg and symmetric anisotropic exchange interactions. Depending on local symmetries and electron hopping pathways these additional interactions may be of comparable strength to the Kitaev term [5]. Dominant Kitaev interactions are known to be present in transition metal compounds with octahedrally coordinated  $5d^5$  and  $4d^5$  electronic filling, including the  $\text{Ir}^{4+}$  oxides and  $\text{Ru}^{3+}$  based chlorides and trihalides [2, 6–14], but strong Heisenberg and anisotropic interactions stabilize Néel order in all of these compounds [5]. It is thus essential to search for other material realizations where the non-Kitaev interaction terms can be further minimized.

Recently, it has been shown that strong Kitaev interactions are potentially realizable in a broader class of materials, including compounds with high spin  $d^7$  electronic configuration such as  $\text{Co}^{2+}$  and  $\text{Ni}^{3+}$  [15, 16], and the  $f^1$  electronic configuration such as  $\text{Ce}^{3+}$  and  $\text{Pr}^{4+}$  [3, 17]. In the case of the  $f^1$  electron materials, a dominant spin-orbit coupling and octahedral crystal field can act to stabilize a  $\Gamma_7$  doublet,  $J_{\text{eff}} = 1/2$ , with strong Kitaev interactions [3, 18]. Furthermore, the more spatially localized  $f$ -orbital occupying electrons compared to those in  $4d$  and  $5d$  orbitals could serve to limit direct exchange interactions.

One candidate material to realize such Kitaev physics is  $\text{Na}_2\text{PrO}_3$ , which hosts octahedrally coordinated  $\text{Pr}^{4+}$  in the  $f^1$  electronic configuration [19].  $\text{Na}_2\text{PrO}_3$  crystallizes in the  $C2/c$  space group with edge-sharing  $\text{PrO}_6$  octahedra, required for the realization of the dominant bond directional exchange [3, 17, 18]. The crystal structure has two inequivalent Pr sites forming a honeycomb lattice in the  $ab$  plane with two in-plane Pr–Pr distances of  $d = 3.433$  and  $d' = 3.458$  Å. Honeycomb planes are separated by layers of Na atoms with an interplane Pr–Pr distance of  $d_p = 5.867$  Å [20, 21]. Based on *ab initio* studies,  $\text{Na}_2\text{PrO}_3$  was predicted to host antiferromagnetic Kitaev interactions between local  $J_{\text{eff}} = 1/2$  moments on  $\text{Pr}^{4+}$  [17, 18]. On the contrary, neutron crystal field measurements revealed that the  $\text{Pr}^{4+}$  ground state wavefunction is not a  $\Gamma_7$  doublet as required for the Kitaev model. Furthermore, the magnetic excitations are best captured by a Heisenberg XXZ model Hamiltonian with negligible Kitaev interactions [21]. Recent neutron and x-ray absorption measurements confirm that the Pr ground state in  $\text{Na}_2\text{PrO}_3$  deviates significantly from the  $\Gamma_7$  doublet as a result of strong octahedral crystal field and  $\text{Pr}(4f)$ – $\text{O}(2p)$  hybridization [21, 22]. However, there are still questions regarding the magnetic ground state of  $\text{Na}_2\text{PrO}_3$ . Despite a clear heat capacity peak at  $T_N$  [19], and the appearance of well defined spin waves, no direct evidence for static magnetic order has been found in this material. Furthermore, an apparent continuum of magnetic excitations existing above the spin wave bands remains unexplained [21]. Together, the conspicuously small static magnetic moment and excitation continuum leave open the possibility for significant quantum fluctuations in  $\text{Na}_2\text{PrO}_3$ .

In this work, we use a comprehensive series of muon spin spectroscopy ( $\mu\text{SR}$ ) and neutron scattering measurements ac-

accompanied by DFT and model Hamiltonian simulations to refine the magnetic ground state and underlying microscopic exchange interactions of  $\text{Na}_2\text{PrO}_3$ . Our results rule out any significant, beyond spin-wave, quantum fluctuations in this material and establish crystal field effects and stacking faults as the primary origin of the small ordered moment. The  $\mu\text{SR}$  measurements unambiguously reveal that  $\text{Na}_2\text{PrO}_3$  is antiferromagnetically ordered below  $T_N \approx 4.9$  K. Analysis of the muon data supplemented with DFT and dipolar simulations find the most likely ordered state to be a Néel AF structure with a small static magnetic moment of  $\mu_{\text{static}} \leq 0.22 \mu_B/\text{Pr}$ , collinearly aligned along the  $c$ -axis. Measurements of the crystal field excitations reveal five additional crystal field modes above the previously reported single crystal field excitation [21]. The full set of crystal fields more tightly constrain the  $\text{Pr}^{4+}$  ground state wavefunction. Low energy inelastic neutron scattering revealed intense single and multi-magnon excitations. The complete measured magnetic excitation spectrum is well described by a non-linear spin wave model in the collinear Néel state that includes a dominant Heisenberg exchange and subdominant symmetric anisotropic exchange interactions. We find that the previously unexplained continuum of magnetic excitations arises from a multi-magnon excitations with relatively large neutron intensity that is accounted for by  $g$ -factor anisotropy. Our analysis demonstrates a small ( $\sim 20\%$ ) ordered moment reduction arising from quantum fluctuations. The fluctuating moment of  $\delta m = \sqrt{g^2 J(J+1) - g^2 J_z^2} = 0.75(14) \mu_B/\text{Pr}$  recovered from the energy and momentum integrated inelastic neutron intensity is reduced from expectations for a local  $J = 1/2$  and  $g_{\text{avg}} = 1.1$  as determined by our crystal field analysis. Based on these results, we attribute the small moment and intense multi-magnon neutron intensity in  $\text{Na}_2\text{PrO}_3$  to crystal field and covalency effects.

The remainder of this paper is organized as follows. After an overview of the methods in Sec. II, we present the  $\mu\text{SR}$  measurements in Sec. III A along with DFT and dipolar simulations of the muon spectra in Sec. III A 1. In Sec. III B we present and analyze the crystal field excitations. Elastic and inelastic neutron scattering are presented in Secs. III C and III D along with a non-linear spin wave modeling of the measured spectrum, that is used to constrain a model Hamiltonian. The summary and conclusions are presented in Sec. IV.

## II. EXPERIMENTAL AND COMPUTATIONAL METHODS

Powder samples of  $\text{Na}_2\text{PrO}_3$  were synthesized via solid-state reactions from  $\text{Na}_2\text{O}_2$  and  $\text{Pr}_6\text{O}_{11}$ . Dry starting reagents were weighed in a metal ratio,  $\text{Na}/\text{Pr} \sim 2.2$ , to account for sodium evaporative losses, ground in an agate mortar and pestle, and pelletized under an argon environment. The prepared materials were enclosed in Ag ampules and heated at  $750^\circ\text{C}$  under dry, flowing oxygen for 36 hours. Samples were furnace-cooled to  $\sim 150^\circ\text{C}$  and immediately transferred to an Argonne glovebox for storage.

$\mu\text{SR}$  measurements were carried out on the GPS spectrometer at the Paul Scherrer Institut, Switzerland. The sample

was packed into aluminium foil inside a glove-box to avoid air contamination and put into a Cu fork inserted into the experimental probe. The measurements were performed both in a weak Transverse Field (TF) mode to calibrate the asymmetry parameter of the muon polarization, and in Zero Field (ZF) to reveal presence of the internal magnetic field that gives rise to the spontaneous oscillations of  $\mu\text{SR}$  signal. The ZF  $\mu\text{SR}$  spectra were collected at temperatures ranging from 1.5 K to 5.2 K using a helium flow cryostat. The time-differential  $\mu\text{SR}$  data were fitted using MUSRFIT software [23], and the MuLab suite, a home-built Matlab toolbox.

To identify the muon implantation sites, we used the well-established DFT+ $\mu$  approach [24–27]. Non-spin polarized DFT calculations were performed within generalized gradient approximation (GGA) for the PBE (Perdew-Burke-Ernzerhof [28]) exchange-correlation functional as implemented in the Quantum Espresso code [29]. The muon was treated as a hydrogen impurity in a  $2 \times 1 \times 1$  charged supercell (96 host atoms and 1 muon) with a compensating background. For Na, O, and H atomic species, the norm-conserving pseudopotentials were used; while for Pr, the Projector augmented wave (PAW) with no  $4f$  electron state in the valence was used, in order to avoid the well-known difficulty in describing its valence shell [30]. The plane-wave cut-off of 100 Ry was used while the Brillouin zone was sampled using a  $4 \times 4 \times 4$  mesh of  $k$ -points [31].

High energy neutron scattering measurements of the crystal field excitations were conducted on the fine-resolution Fermi chopper spectrometer (SEQUOIA) [32] at the Spallation Neutron Source (SNS), Oak Ridge National Lab (ORNL). The polycrystalline sample was loaded into an Aluminum can, and cooled to a base temperature of  $T = 5$  K using a closed cycle cryostat. To cover the full range of crystal field excitations with sufficient resolution, data was collected using the high-flux chopper with fixed incident neutron energies of  $E_i = 60, 150, 300, 700, \text{ and } 2500$  meV.

Low energy neutron scattering measurements were carried out on powder samples using the Multi-Axis Crystal Spectrometer (MACS) at the NIST Center for Neutron Research (NCNR). Elastic ( $E = 0$ ) measurements were conducted with the monochromator in a vertical focusing configuration using neutron energy of 5 meV. Inelastic measurements were carried out using a double-focusing configuration and a fixed final energy of  $E_f = 3.7$  meV with Be and BeO filters before and after the sample, respectively for energy transfers  $\Delta E = E_i - E_f$  below 1.5 meV. For energy transfers above 1.4 meV, we used a Be filter after the sample and no incident beam filter. Data for energy transfers above 1.4 meV was corrected for contamination from high-order harmonics in the incident beam neutron monitor. Measured background signal contributions from the sample environment were subtracted and signal count rates were converted to absolute values of the scattering cross-section using the incoherent signal from the sample integrated over the range  $1.7 \leq Q \leq 2 \text{ \AA}^{-1}$ .

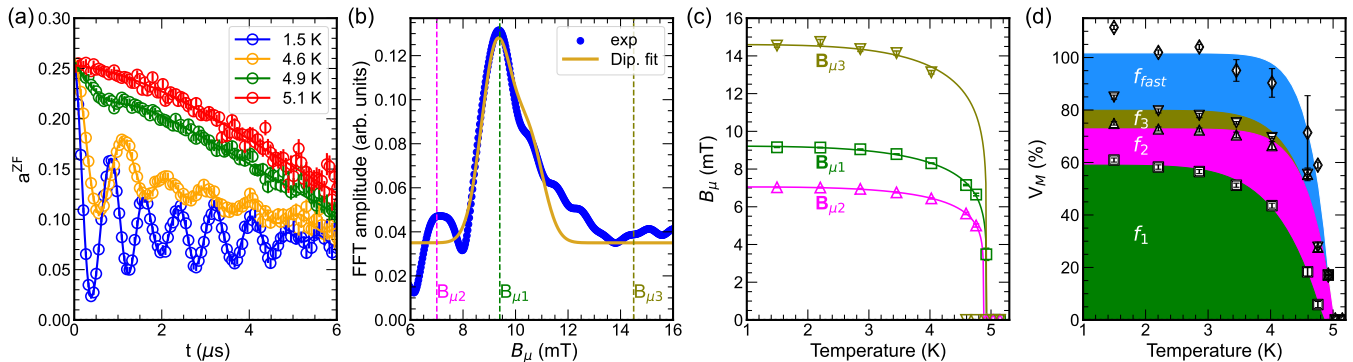


FIG. 1. (Color online) (a) Muon asymmetry spectra at different temperatures. The solid lines are the best fits to the asymmetry data using Eq. 1. (b) The real part of the Fast Fourier Transform (FFT) of the experimental  $\mu$ SR spectrum at  $T = 1.5$  K, with the vertical dashed lines showing the oscillating fields obtained from the best fit of the asymmetry. Solid yellow line is the best fit with the convolution of the computed dipolar fields to a Gaussian distribution with the Néel-I AF magnetic structure (See Fig. 2(c)). The fit gives a magnetic moment size of  $m_{\text{static}} = 0.131 \mu_B$ . (c) The internal fields ( $B_{\mu i}$ ) as a function of temperature. Solid lines are a fit to the power law function described in the text. (d) The magnetic volume fraction  $V_M$  as a function of temperature, color shaded to illustrate the relative contribution of each term in Eq 1.

### III. RESULTS

#### A. Muon spin relaxation ( $\mu$ SR)

The measured ZF  $\mu$ SR asymmetry spectra,  $a^{\text{ZF}}(t)$ , are shown in Fig. 1 (a) for four different temperatures. At temperatures above  $\sim 4.9$  K, the  $\mu$ SR signal shows no oscillations, indicating that the sample is in the paramagnetic phase. Upon lowering the temperature below 4.9 K, the  $\mu$ SR signal displays damped coherent oscillations, indicating the emergence of long-range magnetic order due to the presence of a static internal magnetic field. Furthermore, we also observe a fast relaxation at short times, reflecting presence of static magnetic moments. As the temperature is further lowered to 1.5 K, the signature oscillations of the long-range magnetic order become more pronounced and dominate the  $\mu$ SR spectra.

All observed ZF- $\mu$ SR spectra are well fit with the following model, commonly used to describe  $\mu$ SR asymmetry in antiferromagnets [33];

$$a^{\text{ZF}}(t) = a_0 \left[ \sum_{i=1}^3 f_i e^{-\lambda_i t} \cos(\gamma_\mu B_{\mu,i} t + \phi) + f_{\text{fast}} e^{-\lambda_{\text{fast}} t} + f_l e^{-\lambda_l t} e^{-(\sigma t)^2} \right], \quad (1)$$

where  $a_0$  is the muon initial amplitude calibrated at high temperature. In a powder sample we expect the internal local field  $\mathbf{B}_\mu$  to have both longitudinal and transverse components with respect to the muon spin  $\mathbf{S}_\mu$ . The first term in Eq. 1 describes the transverse components with an exponentially damped oscillating signal that decays with a transverse relaxation rate  $\lambda$ , summed over all muons that thermalize at three symmetrically inequivalent sites. The parameter  $f_i$  controls the contribution of each muon stopping site  $i$  to the total asymmetry signal.  $\gamma_\mu$  ( $= 2\pi \times 135.5 \text{ MHz T}^{-1}$ ) is the muon gyromagnetic ratio,  $B_\mu$  ( $= 2\pi\nu_\mu/\gamma_\mu$ ) is the muon internal magnetic field corresponding to muon precessing with frequency  $\nu_\mu$ , and  $\phi$  is the initial phase.

The second term in Eq. 1 accounts for the transverse component for a site with overdamped oscillations, labeled as fast non-oscillating term, with amplitude  $a_0 f_{\text{fast}}$  and depolarization rate  $\lambda_{\text{fast}}$  ( $\sim 2 \mu\text{s}^{-1}$ ). The third term accounts for the longitudinal component with damped relaxation, amplitude  $a_0 f_l$ , and spin-lattice relaxation rates  $\lambda_l$ . Finally, for  $T \geq T_N$ , static dipolar interactions with nuclear moments with depolarization rate  $\sigma \approx 0.2 \mu\text{s}^{-1}$  dominate the muon spectra.

In Fig. 1 (b), we show the real part of the Fast Fourier Transform (FFT) of the time-domain  $\mu$ SR asymmetry at  $T = 1.5$  K. Three local magnetic fields are identified from the best fit of Eq. 1 to the asymmetry signal at  $T = 1.5$  K. We label these  $B_{\mu 1} = 9$  mT, corresponding to the peak with maximum Fourier power, then  $B_{\mu 2} = 7$  mT, and  $B_{\mu 3} = 15$  mT.

The temperature dependence of the three distinct internal fields  $B_{\mu i}$  are shown in Fig. 1(c). Here the solid lines represent fit to a phenomenological double exponent power-law function;  $B_{\mu i}(T) = B_{\mu i}(0)(1 - (T/T_N)^\alpha)^\beta$  [34, 35]. From this fit, we obtained an estimate of the Néel temperature of  $T_N \approx 4.9$  K, consistent with heat capacity and neutron measurements [19, 21]. The  $\alpha$  exponent accounts for the magnetic excitation at low temperatures while the  $\beta$  exponent reflects the dimensionality of the interactions in the vicinity of the transition. A least squared fit to each internal field component yielded  $\alpha = (3.673 \pm 0.533, 4.078 \pm 0.206, 4.078 \pm 0.206)$  and  $\beta = (0.160 \pm 0.011, 0.147 \pm 0.007, 0.147 \pm 0.007)$  for  $(B_{\mu 1}, B_{\mu 2}, B_{\mu 3})$  respectively. To obtain an estimate of these exponents we take the average, to find  $\alpha = 3.94 \pm 0.20$  and  $\beta = 0.151 \pm 0.005$ . The  $\beta$  value is far less than  $\approx 1/3$  expected for a three-dimensional magnetic Hamiltonian [36]. Its average value is close to that expected for a two-dimensional XXZ model [37]. However, the large  $\alpha$  value indicates presence of complex magnetic interactions [38, 39]. These findings are in agreement with those from neutrons presented below.

We obtained the magnetic volume fraction ( $V_M$ ) from the asymmetry amplitudes extracted from fits to Eq. 1 [40]. Temperature dependent  $V_M$  for each internal field component are

shown in Fig. 1 (d); the fill color denotes the relative contributions of the muon at each distinct stopping site. The signal  $f_1$  corresponds to the muon at site  $A_1$  and contributes 59% to  $V_M$  (green shaded area). Sites  $A_2$  (signal contribution  $f_2$ ) and  $A_3$  (signal contribution  $f_3$ ) contribute 14% and 7% respectively, resulting in a total of 80% contribution to  $V_M$  from implanted muons that are sensitive to the internal magnetic field. The remaining 20% is recovered from the amplitude of the fast non-oscillating relaxing signal ( $f_{\text{fast}}$ ), showing that 20% of the implanted muons do not exhibit coherent precession.

### 1. Muon sites and dipolar field analysis

To characterize the contributions of each muon site to the oscillatory components of the  $\mu\text{SR}$  signal in Fig. 1 (a), and constrain the magnetic structure, we proceed to identify the muon implantation site(s) in  $\text{Na}_2\text{PrO}_3$  using the DFT+ $\mu$  approach. DFT modeling reveals three symmetrically distinct candidate muon sites, consistent with sites  $A_1$ ,  $A_2$ , and  $A_3$  from the analysis of  $\mu\text{SR}$  data above. Each of these sites is located at the 8f Wyckoff position, with a distance of  $\approx 1 \text{ \AA}$  along the  $c$  axis to the three distinct O sites in the unit cell, as shown in Fig. 2 (a) and (b). These sites are found to be in the direction of the non-magnetic Na layer and farther away from the magnetic  $\text{Pr}^{4+}$  ions (Fig. 2 (a)). This is consistent with observations in typical oxide compounds where the positive muon is well known to stop near the O sites [27, 41].

Our DFT calculations predict that the  $A_1$  site has the lowest energy, but the energy differences between  $A_1$ ,  $A_2$ , and  $A_3$  sites are less than 0.2 eV. These findings imply that muons populate the  $A_1$ ,  $A_2$ , and  $A_3$  sites with nearly equal probability.

TABLE I. The best fit magnetic orders labelled Néel-I, Néel-II, A-type, and Stripy, shown in Fig. 2 (c); their propagation vector, Group (BNS), their magnetic moment (m) values and the calculated dipolar field ( $B_{\text{dip}}$ ) at muon sites  $A_1$ ,  $A_2$ , and  $A_3$  using the corresponding magnetic configuration.  $B_{\text{dip}}$  values are to be compared with  $B_{\mu 1} = 9 \text{ mT}$ ,  $B_{\mu 2} = 7 \text{ mT}$  and  $B_{\mu 3} = 15 \text{ mT}$  from experiment.

Label	$k_m$	Group (BNS)	$m_{\text{static}} (\mu_B)$	$B_{\text{dip}}^{A1} (\text{mT})$	$B_{\text{dip}}^{A2} (\text{mT})$	$B_{\text{dip}}^{A3} (\text{mT})$
Néel-I	000	$C2'/c'$ (15.89)	0.131	11	9	9
Néel-II	000	$C2'/c$ (15.87)	0.130	10	10	9
A-type	000	$C2'/c'$ (15.88)	0.212	9	9	10
Stripy	100	$Pc2_1/c$ (14.84) <sup>2</sup>	0.106	9	11	10

With the knowledge of the muon implantation sites, we determined the magnetic structure and ordered moment size in  $\text{Na}_2\text{PrO}_3$  by direct comparison of simulated dipolar field distributions at these site(s) with experimental results. First, by considering the maximal magnetic space groups (MAXMAGN [42]), we have identified and explored twenty-eight (28) AF magnetic structures, within the  $k_m=(000)$ , (110), and (100) propagation vectors that are most likely based on the minimum of the magnetic excitation spectra discussed in Section III D. For each of these magnetic structures, the muon dipolar interactions [43] were computed at the 24 muon sites (i.e., 3 muon sites at each of the 8f Wyckoff positions) as a function of the Pr magnetic moment. The experimentally observed FFT

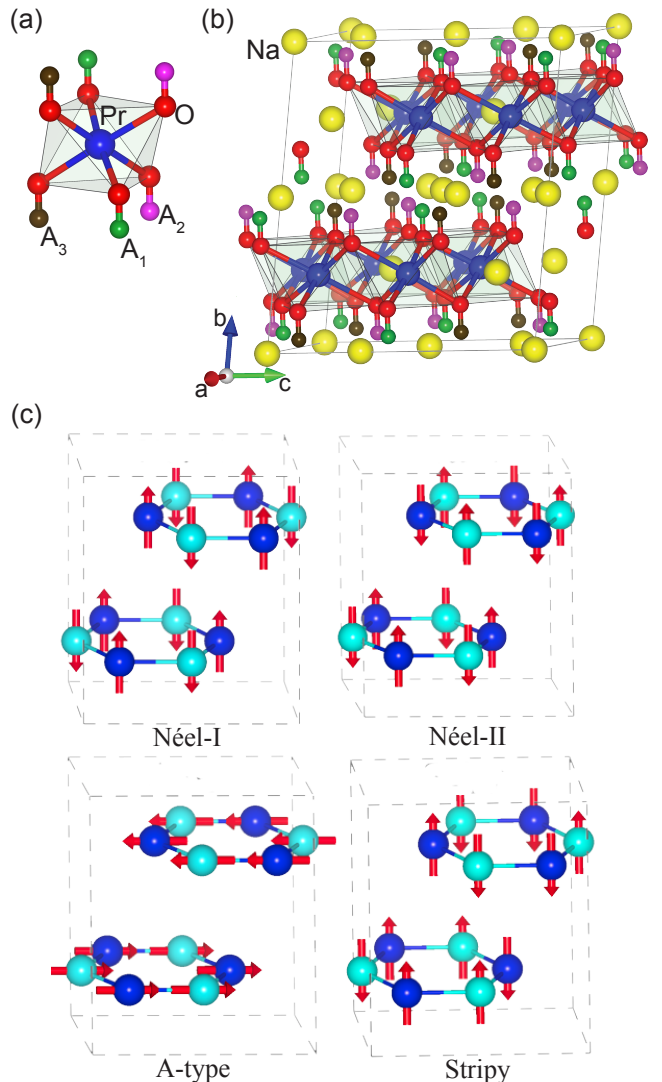


FIG. 2. (a) Muon sites  $A_1$  (green spheres),  $A_2$  (pink) and  $A_3$  (brown) bound to the three O sites of the  $\text{PrO}_6$  octahedra. (b) Muon sites  $A_1$  (green spheres),  $A_2$  (pink), and  $A_3$  (blue) shown in the unit cell of  $\text{Na}_2\text{PrO}_3$  with lattice parameters  $a = 5.96 \text{ \AA}$ ,  $b = 10.32 \text{ \AA}$ ,  $c = 11.73 \text{ \AA}$ ,  $\beta = 109.96^\circ$  [20]. (c) Four proposed AF magnetic structures from analysis of  $\mu\text{SR}$  data, labelled Néel-I, Néel-II, A-type, and Stripy. Only the Pr atoms are shown for clarity (with  $\text{Pr}_1$  dark blue spheres and  $\text{Pr}_2$  sky blue spheres).

power spectrum at 1.5 K (Fig 1 (b)) was then fit to the convolution of the computed dipolar fields and a Gaussian distribution (See Appendix Sec. A). The  $\mu\text{SR}$  magnetic structural analysis identified four possible AF magnetic structures, labeled Néel-I, Néel-II, A-type, and Stripy in Fig. 2 (c), that are consistent with our experimental findings. We found that the fit to the Néel-I AF structure with magnetic moments aligned parallel to the crystal  $c$ -axis gives the best matching dipolar field distribution shown in Fig. 1(b). We point out that this magnetic configuration is also in agreement with the analysis of the neutron data, as we discuss below. Furthermore, as shown in Table I, the effective static magnetic moment size determined from

the best fit to the real FFT spectrum are notably very small,  $m_{\text{static}} < 0.22 \mu_B/\text{Pr}$ .

## B. Crystal Field Excitations

In order to elucidate the magnetic degrees of freedom in  $\text{Na}_2\text{PrO}_3$ , we first present an analysis of crystal field excitations. Fig. 3 (a) shows the low temperature (5 K) inelastic neutron scattering (INS) contour plots with incident energy  $E_i = 700$  meV, which clearly reveals at least four inelastic features with intensities that decrease with increasing momentum transfer, consistent with crystal field excitations at  $\sim 250, 300, 400$  and  $500$  meV. The additional local excitation that appears at  $452$  meV has an intensity that increases with momentum transfer indicating that it is of nuclear origin. We identify this feature with an O-H stretching mode [44, 45]. The low  $Q$  magnetic intensity exists on a large high energy background with dispersion that is characteristic of a hydrogen recoil, providing further evidence of the presence of hydrogen contamination that likely originates from a brief exposure of the sample to atmosphere during synthesis. Such O-H stretching modes and hydrogen recoil scattering were also apparent in previous studies of  $\text{Na}_2\text{PrO}_3$  [21]. We note that bulk characterization of our sample as well as neutron diffraction and inelastic scattering presented below are consistent with previous reports, demonstrating that this small amount of hydrogen present has negligible effect on the sample properties.

To better resolve the intrinsic crystal field excitations from the large background signal, we integrate the neutron data over  $|Q| = [6, 11] \text{ \AA}^{-1}$  and fit a background signal using a decaying exponential with an additional Gaussian centered on the  $450$  meV O-H stretching mode as shown in Fig. 3 (b). This background was subtracted to produce the data shown in Fig. 3 (c), while the higher resolution  $E_i = 300$  meV data shown in Fig. 3 (d) revealed that the crystal field intensity spectrum below  $250$  meV is comprised of two modes around  $\sim 230$  and  $\sim 240$  meV. No additional crystal field modes were found at higher energies for data collected using neutron incident energies (up to  $2.5$  eV). To obtain the peak positions, we fit the INS data to a Voigt profile after subtracting a large background (see Fig. 3 (b)). In total, six CEF excitations were revealed at energies of  $228, 243, 296, 388, 528$  and  $568$  meV. The first two modes, at  $228$  and  $243$  meV are consistent with prior studies that found a single broad energy mode centered at  $233$  meV [21, 22], but our higher energy resolution clearly shows that this mode is split, while an improved signal to noise unveils four additional crystal field modes that were not previously visible above background.

The six crystal field excitations we observe are consistent with the previously proposed intermediate coupling scheme for  $\text{Na}_2\text{PrO}_3$  [22], confirming the importance of crystal electric field (CEF) interactions in  $\text{Na}_2\text{PrO}_3$ . However, the higher quality of our data allows us to better constrain microscopic parameters by fitting solely the crystal field level energies and intensities.

We computed  $\text{Pr}^{4+}$  single ion crystal electric field (CEF) Hamiltonian ( $H_{CEF}$ ) from a point charge (PC) model within

the intermediate coupling regime using the following CEF Hamiltonian [46]

$$H_{CEF} = B_2^0 O_2^0 + B_2^{\pm 2} O_2^{\pm 2} + B_4^0 O_4^0 + B_4^{\pm 2} O_4^{\pm 2} + B_4^{\pm 4} O_4^{\pm 4} + B_6^0 O_6^0 + B_6^{\pm 2} O_6^{\pm 2} + B_6^{\pm 4} O_6^{\pm 4} + B_6^{\pm 6} O_6^{\pm 6}, \quad (2)$$

where  $B_n^{\pm m}$  are the CEF parameters and  $O_n^{\pm m}$  are the Stevens Operators.  $H_{CEF}$  includes contributions from the non-zero  $-m$  components that are *imaginary* in the Stevens Operators and second order terms. Both are required to account for the low symmetry Pr ion local environment [22]. We also found that fourth and sixth order terms were required to capture all observed crystal field excitations, especially at higher energy. For our calculations, we considered  $\text{Pr}^{4+}$  ion with orbital angular momentum  $L = 3$ , spin quantum number  $S = 1/2$ , represented by isoelectronic  $\text{Ce}^{3+}$  ion. We obtained reasonable fits of the PC model to the INS data varying the spin orbit coupling strength of between  $40$  and  $60$  meV and we report the best fit results for  $\lambda = 54$  meV.

Our model calculations were initialized by generating the PC model to provide a set of starting CEF parameters that were further refined through least-squares fitting to the  $E_i = 700$  meV INS data. The first column of Table II presents the values of the CEF parameters  $B_n^{\pm m}$  from the PC model, while the second column presents the final optimized CEF parameters. A notable feature from the obtained CEF parameters is that significant sixth order terms are required to capture all features of the excitations.

TABLE II.  $B_n^{\pm m}$  values in meV obtained from the PC model (first column), and fit of the obtained PC model parameters to the INS data at  $E_i = 700$  meV.

$B_n^{\pm m}$	PC	PC fit
$B_2^0$	-2.1967	6.3207
$B_2^{\pm 2}$	-10.4081	-2.3956
$B_2^{-2}$	2.3018	10.1864
$B_4^0$	-0.0800	-0.0057
$B_4^{\pm 2}$	-0.4789	-0.2748
$B_4^{-2}$	-1.6177	-1.1675
$B_4^{\pm 4}$	-0.7456	-0.0317
$B_4^{-4}$	0.8509	0.1006
$B_6^0$	0.0080	-0.0313
$B_6^{\pm 2}$	-0.0100	0.0890
$B_6^{-2}$	-0.0032	-0.0121
$B_6^{\pm 4}$	0.0625	-0.0065
$B_6^{-4}$	0.0001	0.1596
$B_6^{\pm 6}$	0.0665	0.1956
$B_6^{-6}$	-0.0140	-0.2250

Fig. 3 (c) displays a comparison of the INS intensity with the PC model fit (brown dashed line) that provides excellent agreement with all six observed excitations. The ground state eigenvectors in the  $|L, S\rangle$  basis resulting from the PC model fit are reported in Table III, while the complete eigenvalues and eigenvectors can be found in the Supplemental Material [47]. The low symmetry local environment of  $\text{Pr}^{4+}$  results in a ground state wavefunction that deviates significantly from the  $\Gamma_7$  doublet [17, 18]. Furthermore, we find a mixed ground state, with

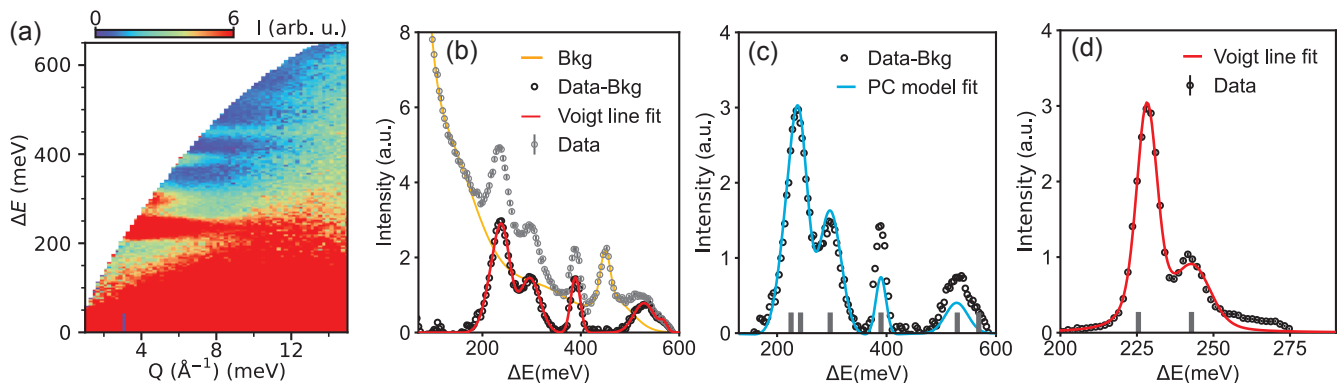


FIG. 3. (a)  $E_i = 700$  meV inelastic neutron scattering signal in  $\text{Na}_2\text{PrO}_3$ . (b) Constant momentum transfer cut from  $E_i = 700$  meV data integrated over  $|Q| = [6, 11] \text{ \AA}^{-1}$ . A background arising from phonons, vibrational excitations and H scattering was subtracted prior to analysis of the crystal field features. (c) Point charge model fit to  $E_i = 700$  meV INS spectrum. Vertical bars correspond to the transition levels obtained from the PC model fit. (d) Constant momentum cut from  $E_i = 300$  meV data integrated over  $|Q| = [6, 11] \text{ \AA}^{-1}$  demonstrating two crystal field levels.

TABLE III. The ground state eigenvalue (along the first row) and the corresponding coefficients of the eigen-kets (in the  $|m_l, m_s\rangle$  basis) of the fourteen (14) basis sets from the mixing of the  $f$  orbitals (down the column), obtained from the point-charge model fit to INS data.

$\Delta E$ (meV) $\rightarrow$	0.000	0.000
$ -3, -\frac{1}{2}\rangle$	(-0.086+0i)	0i
$ -3, \frac{1}{2}\rangle$	0i	(0.143+0i)
$ -2, -\frac{1}{2}\rangle$	0i	(0.017-0.027j)
$ -2, \frac{1}{2}\rangle$	(0.155+0.163i)	0i
$ -1, -\frac{1}{2}\rangle$	(-0.346-0.478i)	0i
$ -1, \frac{1}{2}\rangle$	0i	(0.444+0.562i)
$ 0, -\frac{1}{2}\rangle$	0i	(-0.17-0.173i)
$ 0, \frac{1}{2}\rangle$	(0.17-0.173i)	0i
$ 1, -\frac{1}{2}\rangle$	(-0.443+0.563i)	0i
$ 1, \frac{1}{2}\rangle$	0i	(0.345-0.479i)
$ 2, -\frac{1}{2}\rangle$	0i	(-0.155+0.163i)
$ 2, \frac{1}{2}\rangle$	(-0.017-0.027i)	0i
$ 3, -\frac{1}{2}\rangle$	(-0.143+0i)	0i
$ 3, \frac{1}{2}\rangle$	0i	(0.086-0i)

significant contribution from the  $j = 5/2$  and  $j = 7/2$  multiplets. The coefficients of all the 14-fold degenerate basis are non-vanishing, as shown in Table III. The complexity of the ground state wavefunction reflects the low symmetry of the Pr local environment and likely significant hybridization between Pr ( $4f$ ) and O ( $2p$ ) states so that a point charge crystal model provides only an effective description of the magnetism in  $\text{Na}_2\text{PrO}_3$ . This conclusion is consistent with recent x-ray absorption spectroscopy measurements [22] and with a reduced local moment as revealed by our  $\mu\text{SR}$  and neutron scattering measurements presented below.

The observed  $g$ -tensor is anisotropic with average transverse components in the honeycomb plane components  $g_{\pm} = 1.05$  and a longitudinal component of  $g_z = 1.35$ , with  $g_z/g_{\pm} = 1.29$ . These illustrate that the CEF effects introduce an easy axis anisotropy that is consistent with a  $c$ -axis oriented ordered moment.

### C. Neutron Diffraction

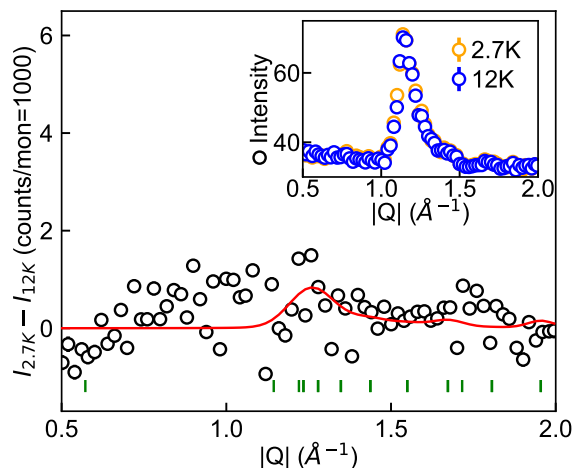


FIG. 4. Elastic neutron scattering at  $T=2.7$  K, well below  $T_N$ , and 12 K, well above  $T_N$  (inset) and the difference between the 2.7 K, and 12 K. The red line is the simulated diffraction pattern for a Néel-I order with a moment size of  $0.3 \mu_B$ . Expected Bragg peak positions are indicated by the green ticks.

Both heat capacity [19] and our  $\mu\text{SR}$  measurements indicate that  $\text{Na}_2\text{PrO}_3$  undergoes long-range magnetic ordering below  $T_N = 4.9$  K, this ordered state should give rise to a magnetic Bragg reflection visible with neutron diffraction. Fig. 4 shows the elastic neutron signal measured at  $T = 2.7$  K and  $T = 12$  K. To place tight constraints on any ordered magnetic moment, we plot the difference between  $T = 2.7$  and 12 K. The difference data do not show any evidence for magnetic Bragg intensity or diffuse scattering above the statistical noise indicating that any three dimensional ordered moment in  $\text{Na}_2\text{PrO}_3$  is extremely small, consistent with the  $\mu\text{SR}$  analysis presented above and previous reports [21]. The variance of the difference data places an upper bound on the ordered moment of  $m \leq 0.3 \mu_B$

assuming a three-dimensional ordered Néel-I magnetic structure with moments aligned along the  $c$ -axis, consistent with the  $\mu$ SR and inelastic neutron spectra described below. This upper bound represents a significantly reduced moment compared with expectations from the  $J = 1/2$  ground state doublet and  $g_z=1.35$  from our crystal field analysis, giving  $m_z \approx 0.65 \mu_B$ .

Although  $\mu$ SR clearly reveals a static, ordered, moment below  $T_N$  in  $\text{Na}_2\text{PrO}_3$ , both  $\mu$ SR and elastic neutron scattering find that this ordered moment is vanishingly small. There are three most likely, and not mutually exclusive, possibilities for such a small ordered moment. The first possibility is the presence of structural disorder that inhibits the formation of three-dimensional long-range order. In particular, stacking faults that are known to be prevalent in  $\text{Na}_2\text{PrO}_3$  [20]. The presence of such stacking faults would increase the upper bound on the ordered moment size determined by neutron diffraction. The second possibility is significant Pr–O covalency that results in a fraction of the moment on the O site. The third is presence of significant quantum fluctuations that reduce the ordered moment size. Such fluctuations would be expected to arise from a frustrated magnetic Hamiltonian. Since quantum fluctuations of the ordered moment act to shift magnetic neutron intensity from the elastic ( $E = 0$ ) channels to inelastic ones, the possible presence of significant quantum fluctuations is directly testable through analysis of the low energy magnetic excitation spectra as we will discuss below.

#### D. Magnetic Excitations

The measured powder averaged low energy ( $\delta E < 10$  meV) inelastic neutron scattering for  $\text{Na}_2\text{PrO}_3$  is shown in Fig. 5 (a). There are two visible branches of magnetic excitations, centered at 1.5 and 3 meV. The lower energy branch exhibits a clear dispersion, with a 1 meV gap and 1.5 meV bandwidth consistent with previous reports [21]. Excitations disperse from a minimum energy at  $Q = 1.25 \text{ \AA}^{-1}$  corresponding to the (110) Bragg position as expected for spin waves in the Néel-I ordered state. The higher energy branch of magnetic excitations is centered around 3.2 meV and extends into a continuum up to 5 meV, most clearly visible in the constant momentum transfer cut of Fig. 5 (c). Given that this high energy branch intensity is maximum at approximately twice the energy of the lower energy zone boundary – where the density of single magnon states is maximized – and the intensity of the higher energy branch is significantly reduced with respect to the lower energy one, we associate the higher energy excitations with a multi-magnon continuum. Such an assignment is supported by non-linear spin wave modeling discussed below. Both branches of magnetic excitations follow the same temperature dependence, collapsing into a broad energy continuum of the paramagnetic response above  $T_N$ .

To model the magnetic excitations in the Néel state, we consider the generic nearest-neighbour model for Kramer's pseudo-spins on the honeycomb lattice. This includes four

symmetry allowed exchange interactions [5, 48],

$$\sum_{\langle ij \rangle_\mu} \left[ JS_i \cdot S_j + KS_i^\mu S_j^\mu + \Gamma (S_i^\nu S_j^\rho + S_i^\rho S_j^\nu) + \Gamma' (S_i^\mu S_j^\rho + S_i^\rho S_j^\mu + S_i^\nu S_j^\nu + S_i^\nu S_j^\mu) \right],$$

where  $\langle ij \rangle_\mu$  is a  $\mu$ -type bonds and  $\mu\nu\rho$  are a permutation of the octahedral axes  $xyz$ . This includes the Heisenberg exchange  $J$ , Kitaev exchange  $K$  and two symmetric off-diagonal exchanges  $\Gamma$  and  $\Gamma'$ . We will assume the strictly crystallographically inequivalent nearest neighbor bonds have the same exchange interactions, effectively granting the model three-fold rotation symmetry about the  $c$ -axis. We do not include  $c$ -axis exchange interactions as these are expected to be weak and minimally influence the powder averaged dynamical structure factor.

We have assumed the  $J = 1/2$  pseudo-spins in  $\text{Na}_2\text{PrO}_3$  are defined with respect to the local cubic axes. Alternatively, a trigonal basis that quantizes the spins along the out-of-plane and high-symmetry in-plane directions can be used and yields [49, 50]

$$\sum_{\langle ij \rangle} \left[ J_1 (S_i^x S_j^x + S_i^y S_j^y + \Delta S_i^z S_j^z) + J_{\pm\pm} (\gamma_{ij} S_i^+ S_j^+ + \text{h.c.}) - J_{z\pm} (\gamma_{ij}^* [S_i^+ S_j^z + S_i^z S_j^+] + \text{h.c.}) \right],$$

where  $\gamma_{ij}$  are bond dependent phase factors ( $\gamma_x = 1$ ,  $\gamma_y = \omega$ , and  $\gamma_z = \omega^*$  where  $\omega = e^{2\pi i/3}$ ).

Classically, a Néel state can be stabilized on the honeycomb lattice by a dominant anti-ferromagnetic exchange  $J > 0$ , leaving the staggered moment direction arbitrary. Including a Kitaev interaction in addition to the Heisenberg interaction stabilizes a staggered moment aligned along one of the cubic axes through an order-by-quantum-disorder mechanism. Finite symmetric off-diagonal exchanges will select a direction even classically, with  $\Gamma + 2\Gamma' > 0$  favoring out of the honeycomb plane, corresponding to  $\Delta > 1$  in the trigonal basis, and  $\Gamma + 2\Gamma' < 0$ , corresponding to  $\Delta < 1$ , favoring an in-plane staggered moment – the in-plane direction is unfixed classically, but will be selected via order-by-disorder [51]. We assume the staggered moment orientation is selected by the symmetric off-diagonal exchanges given the small selection energy of the order-by-disorder mechanism and fix  $\Gamma + 2\Gamma' > 0$  to yield a staggered moment oriented out of the honeycomb plane, consistent with expectations from  $\mu$ SR.

The magnetic excitations in the Néel phase can be calculated semi-classically using spin-wave theory. We carried out calculations of the powder-averaged dynamical structure factor for several sets of exchange constants ( $J, K, \Gamma, \Gamma'$ ) including the XXZ limits (only  $J_1, \Delta$  non-zero) and the  $J - \Gamma - \Gamma'$  model (setting  $K = 0$ ). We note that the XXZ limit is equivalent to  $K = 0$  and  $\Gamma = \Gamma'$  with  $J_1 = J - \Gamma$  and  $\Delta J_1 = J + 2\Gamma$ . Given the small ordered moment we have included corrections to linear spin wave theory up to order  $O(1/S^2)$  to ensure we can capture any quantum fluctuations. Details of the formalism for these non-linear spin-wave theory calculations can be found (e.g.) in Refs. [51–53].

First, we note that large gap observed experimentally can be captured even in linear spin-wave theory with three-fold

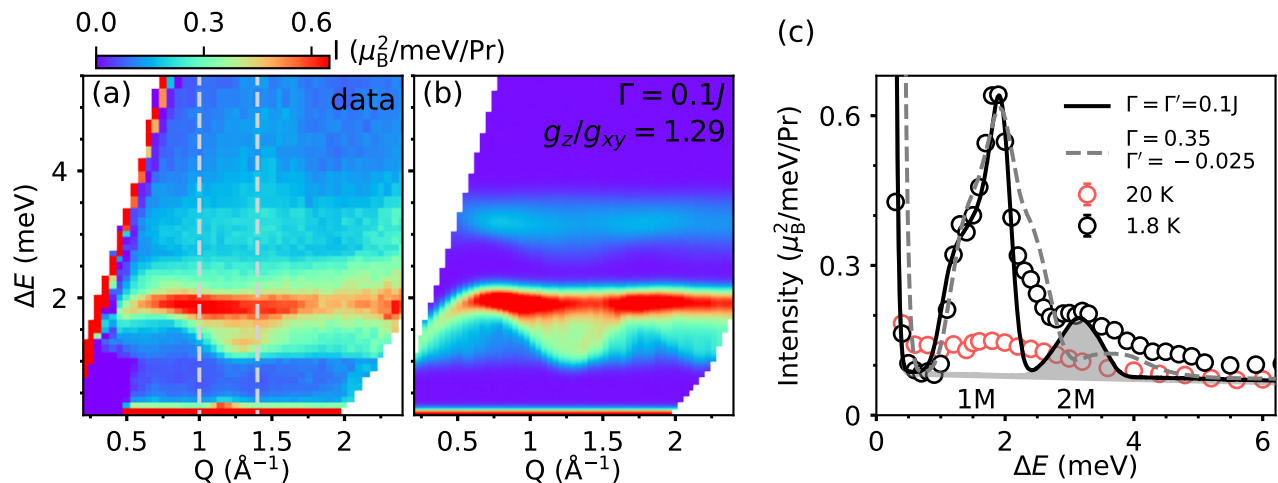


FIG. 5. (a) Inelastic neutron scattering data for  $\text{Na}_2\text{PrO}_3$  at  $T = 1.8$  K. (b) Simulated powder averaged non-linear spin wave spectrum for the  $J$ - $\Gamma$  model with  $J=1$  meV and  $\Gamma = \Gamma' = 0.1J$  corresponding to the XXZ limit. (c)  $T = 1.8$  and 20 K constant momentum transfer cut integrated between  $1 < Q < 1.4 \text{ \AA}^{-1}$ , as indicated by dashed lines in (a). Solid line shows the non-linear spin wave model as in (b) with the single (1M) and two-magnon (2M) contributions labelled. Dashed line is the non-linear spin wave model for  $J = 1.24$ ,  $\Gamma = 0.35J$ ,  $\Gamma' = -0.025J$ .

symmetry once  $\Gamma$  and  $\Gamma'$  interactions are included (or equivalently, once  $\Delta \neq 1$ ). Quantitatively, the size of the gap, and the bandwidth of excitations, can be accounted for by several different sets of exchange parameters. The key features of the spectrum are largely determined by the value of  $\Gamma + 2\Gamma'$  (where  $J$  is fixed to set the overall energy scale). Tuning the precise values of  $\Gamma$  or  $\Gamma'$  separately only introduces subtle changes to the powder-averaged intensity that our data cannot constrain. Based on these gross features, we confine our calculations to the value  $\Gamma + 2\Gamma' = 0.3J$ , fixing the scale of the gap relative to the bandwidth, and vary the relative contributions of  $\Gamma$ ,  $\Gamma'$ . Small differences can be observed in the “flatness” of the top of the excitation band and in the distribution of intensities near maxima at  $|\mathbf{Q}| \sim 1 \text{ \AA}^{-1}$  and  $1.75 \text{ \AA}^{-1}$  depending on the precise values used.

To model  $\text{Na}_2\text{PrO}_3$  we considered several cases:  $\Gamma/J = 0.0, 0.1, 0.2, 0.3$  and  $0.35$  holding  $\Gamma'/J = (0.3 - \Gamma/J)/2$  for each to fix  $\Gamma + 2\Gamma'$ . This includes the XXZ limit where  $\Gamma = \Gamma' = 0.1J$  corresponding to  $\Delta = 1.33$  in the trigonal basis, close to the value considered in Ref. [21]. A comparison of this model to the experimental data is shown in Fig. 5 (b) and (c). The theoretical result incorporates up to the  $O(1/S^2)$  contributions of the transverse, longitudinal and transverse-longitudinal parts of the structure factor (which include the leading contribution from the two-magnon continuum) [54, 55]. The overall intensity scale is left arbitrary and a  $g$ -factor anisotropy of  $g_z/g_{\pm} \approx 1.29$  was used. Due to the limited range of  $|\mathbf{Q}|$ , the neutron form factor for  $\text{Pr}^{4+}$  was not included.

Overall the  $J - \Gamma$  model with  $J=1$  meV,  $\Gamma/J = -0.1$ , and  $\Gamma' = \Gamma$  provides an excellent description of the data given the simplicity of the model. We found no improvement moving away from the XXZ limit or including an additional Kitaev exchange. Including the symmetry inequivalent nearest neighbor exchange and out-of-plane exchange interactions will likely lead to an improved description of the data, but our powder

averaged data set is not sufficient to constrain such a large parameter space and the minimal  $J - \Gamma$  model presented here captures the essential physics. Single crystal measurements are required for any reliable further refinement of additional parameters in the magnetic Hamiltonian, to capture the magnetic intensity around  $\Delta E = 2.5$  meV and above 4 meV.

A key feature of the magnetic excitations is the pronounced continuum with a maximum intensity visible near  $\delta E = 3$  meV. Given the powder-averaging, it is tempting to attribute this to an additional band arising due to Kitaev or additional anisotropic interactions. A simpler explanation is that it represents the contribution from the two-magnon continuum associated with the lower energy single magnon band. Kinematically, this is sensible, since the continuum starts above twice the gap, but its unusually high intensity merits further discussion.

Since the two-magnon intensity is determined by components of the spin along the direction of the ordered moment, any reduction of the ordered moment that results from quantum fluctuations must be accounted for by an enhanced two magnon signal. For the XXZ model most relevant to  $\text{Na}_2\text{PrO}_3$  we expect only a modest 20% ordered moment reduction including corrections up to second order, as found in Ref. [56]. Indeed, such a modest moment reduction is anticipated from the data directly, as the large measured spin wave gap relative to the bandwidth acts to energetically “freeze out” moment fluctuations at low temperatures. We conclude that rather than enhanced quantum fluctuations, the strong two-magnon intensity in  $\text{Na}_2\text{PrO}_3$  is a result of  $g$ -factor anisotropy in  $\text{Na}_2\text{PrO}_3$ .

While the one-magnon intensity is determined by the spin components transverse to the ordered moment, and thus are  $\propto g_{\pm}^2$ , the two-magnon intensity is sensitive to the longitudinal component and carries a factor of  $g_z^2$ . The measured  $g$ -factor ratio  $g_z/g_{\pm} \approx 1.29$  thus provides an enhancement of the two-magnon intensity of  $(g_z/g_{\pm})^2 \approx 1.66$  relative to the one magnon intensity. Comparison of the non-linear spin wave

dynamic structure factor with our data in Fig. 5 (c) shows excellent agreement of the relative two magnon intensity with the measured signal at 3 meV.

Despite the apparently small static moment and absence of any magnetic Bragg signal, the inelastic spectra displays well-formed magnon excitations that can be described to a high fidelity with non-linear spin wave theory predicting a modest,  $\sim 20\%$  ordered moment reduction from quantum fluctuations. In the absence of significant quantum fluctuations, the unobservable magnetic Bragg intensity in the powder averaged diffraction data could be accounted for by stacking faults that disrupt three-dimensional magnetic order, allowing long-range order to form in two-dimensional honeycomb planes but only short range order between the planes. The resulting magnetic correlations form “rods” of elastic scattering extending along the  $c^*$  direction. When powder averaged, the rods result in a diffuse signal that is not visible above background. Since the magnetic interactions along the  $c$ -axis are weak, the magnetic excitations do not disperse along this direction and the powder averaged inelastic neutron intensity is not significantly influenced by stacking faults. However, such a scenario cannot account for the small static moment determined by  $\mu$ SR.

The inelastic neutron scattering signal provides an additional, independent check, of the magnetic moment size in  $\text{Na}_2\text{PrO}_3$  through the total moment sum rule. Integrating the total measured inelastic magnetic neutron intensity over the region  $0.7 < \Delta E < 6$  meV and  $0.8 < Q < 1.94 \text{ \AA}^{-1}$ , we obtain an approximate total fluctuating moment of  $\delta m^2 = 3/2 \mu_B^2 \int \int Q^2 I(Q, E) dQ dE / \int Q^2 dQ = 0.57(22) \mu_B^2/\text{Pr}$ . This value accounts for a large systematic error arising from background determination and is reduced from the value of  $\delta m_{\text{local}}^2 = g_{\text{avg}}^2 J(J+1) - \delta_z^2 g_z^2 J_z^2 = 0.7 \mu_B^2/\text{Pr}$  expected for a local  $J = 1/2$  moment and  $g$ -factors as determined by crystal field analysis. The factor  $\delta_z = 0.8$  accounts for a static moment reduction from quantum fluctuations. Such a reduced fluctuating moment demonstrates the absence of significant quantum fluctuations and is consistent with  $m_{\text{static}} \leq 0.2 \mu_B$  determined by  $\mu$ SR. Overall,  $\mu$ SR, neutron crystal field measurements, neutron diffraction, and low energy inelastic scattering reveal that  $\text{Na}_2\text{PrO}_3$  is a well ordered Néel antiferromagnet, exhibiting minimal quantum fluctuations, but there is a large moment reduction from crystal field effects that give rise to a small, anisotropic,  $g$ -factor and covalency that reduces the moment from the single ion limit.

#### IV. SUMMARY AND CONCLUSIONS

Our combined neutron and  $\mu$ SR measurements have demonstrated that  $\text{Na}_2\text{PrO}_3$  is Néel antiferromagnet and well described by a two dimensional  $J - \Gamma$  or equivalently  $XXZ$  model Hamiltonian. Although no magnetic Bragg reflection corresponding to long-range order has been identified,  $\mu$ SR measurements reveal clear oscillations characteristic of long-range order. DFT modeling enabled us to identify the muon stopping sites and compare measured internal field distributions against possible magnetic structures. We find the  $\mu$ SR internal field distribution is most consistent with Néel order with a small

( $\leq 0.22 \mu_B$ ) static moment. Non-linear spin wave modeling of the observed collective magnetic excitations capture the complete spectra. An intense two-magnon band is accounted for through  $g$ -factor anisotropy that acts to enhance the neutron intensity of the longitudinal two-magnon excitations relative to the transverse single magnons, by a factor of  $(g_z/g_{\pm})^2 \sim 1.66$ . We find minimal reduction of the ordered moment from frustration or quantum fluctuations as confirmed through an analysis of the total magnetic spectral weight from inelastic neutron scattering. Overall our work emphasizes how local atomic physics can generate small static magnetic moments and intense multi-magnon continuum observed by inelastic neutron scattering experiments, even in the absence of appreciable quantum fluctuations. Furthermore, our work demonstrates the importance of  $\mu$ SR as a technique for investigating frustrated magnets with small moments and the clear synergies between  $\mu$ SR and INS.

#### V. ACKNOWLEDGEMENTS

K.W.P and Q.W. were supported by the U.S. Department of Energy, Office of Basic Energy Sciences, under Grant No. DE-SC0021223. VFM was supported by the National Science Foundation under grant No. DMR-1905532. JGR was supported by the Natural Sciences and Engineering Research Council of Canada (NSERC) (Funding Reference No. RGPIN-2020-04970). Access to MACS was provided by the Center for High Resolution Neutron Scattering, a partnership between the National Institute of Standards and Technology and the National Science Foundation under Agreement No. DMR-1508249. A portion of this research used resources at the Spallation Neutron Source, a DOE Office of Science User Facility operated by the Oak Ridge National Laboratory. IJO and PB acknowledge financial support from PNRN MUR project ECS-00000033-ECOSISTER and also acknowledge computing resources provided by the STFC scientific computing department’s SCARF cluster and CINECA award under the IS-CRA (Project ID IsCa4) initiative.

#### Appendix A: Magnetic structure determination and $\mu$ SR dipolar field simulations

The search for the magnetic structure in  $\text{Na}_2\text{PrO}_3$  was initialized by considering all possible magnetic configurations for  $k_m = (0, 0, 0)$ ,  $(1, 1, 0)$ , and  $(1, 0, 0)$  propagation vectors and its crystal structure. In Table IV we have listed the maximal magnetic space groups and magnetic configurations that we have obtained utilizing the MAXMAGN [42].

Starting from these maximal magnetic space groups in Table IV, we have considered only antiferromagnetic structures with the following conditions of the magnetic moments; (i)  $m_x = m_z = \sqrt{2}/2|m|$ , (ii)  $m_x = |m|$  and  $m_z = 0$ ; (iii)  $m_x = 0$  and  $m_z = |m|$ , (iv)  $m_y = |m|$  and (v) taking into account two distinct Pr sites, such that for cases i to iv above, we have considered that the moments on  $\text{Pr}_1$  is antiparallel to those on  $\text{Pr}_2$ . Implementing these conditions, we obtained a total of 28 possible magnetic structures. Due to the magnetic symme-

TABLE IV. Magnetic structures from MAXMAGN - Bilbao Crystallographic Server [42]: Maximal magnetic space groups for a given propagation vector  $k_m$ , with two magnetic Pr atoms, Pr1 and Pr2.

$k_m$	Group (BNS)	Magnetic Structure <sup>a</sup>
000	C2'/c' (15.89)	Pr <sub>1</sub> : (m <sub>x</sub> , 0, m <sub>z</sub> ), (m <sub>x</sub> , 0, m <sub>z</sub> ), (m <sub>x</sub> , 0, m <sub>z</sub> ), (m <sub>x</sub> , 0, m <sub>z</sub> ) Pr <sub>2</sub> : (m <sub>x</sub> , 0, m <sub>z</sub> ), (m <sub>x</sub> , 0, m <sub>z</sub> ), (m <sub>x</sub> , 0, m <sub>z</sub> ), (m <sub>x</sub> , 0, m <sub>z</sub> )
	C2/c' (15.88)	Pr <sub>1</sub> : (0, m <sub>y</sub> , 0), (0, -m <sub>y</sub> , 0), (0, m <sub>y</sub> , 0), (0, -m <sub>y</sub> , 0) Pr <sub>2</sub> : (0, m <sub>y</sub> , 0), (0, -m <sub>y</sub> , 0), (0, m <sub>y</sub> , 0), (0, -m <sub>y</sub> , 0)
	C2'/c (15.87)	Pr <sub>1</sub> : (m <sub>x</sub> , 0, m <sub>z</sub> ), (-m <sub>x</sub> , 0, -m <sub>z</sub> ), (m <sub>x</sub> , 0, m <sub>z</sub> ), (-m <sub>x</sub> , 0, -m <sub>z</sub> ) Pr <sub>2</sub> : (m <sub>x</sub> , 0, m <sub>z</sub> ), (-m <sub>x</sub> , 0, -m <sub>z</sub> ), (m <sub>x</sub> , 0, m <sub>z</sub> ), (-m <sub>x</sub> , 0, -m <sub>z</sub> )
	C2/c (15.85)	Pr <sub>1</sub> : (0, m <sub>y</sub> , 0), (0, m <sub>y</sub> , 0), (0, m <sub>y</sub> , 0), (0, m <sub>y</sub> , 0) Pr <sub>2</sub> : (0, m <sub>y</sub> , 0), (0, m <sub>y</sub> , 0), (0, m <sub>y</sub> , 0), (0, m <sub>y</sub> , 0)
100	Pc2 <sub>1</sub> /c (14.84)	Pr <sub>1</sub> : (m <sub>x</sub> , 0, m <sub>z</sub> ), (m <sub>x</sub> , 0, m <sub>z</sub> ), (-m <sub>x</sub> , 0, -m <sub>z</sub> ), (-m <sub>x</sub> , 0, -m <sub>z</sub> ) Pr <sub>2</sub> : (m <sub>x</sub> , 0, m <sub>z</sub> ), (m <sub>x</sub> , 0, m <sub>z</sub> ), (-m <sub>x</sub> , 0, -m <sub>z</sub> ), (-m <sub>x</sub> , 0, -m <sub>z</sub> )
	Pc2 <sub>1</sub> /c (14.84)	Pr <sub>1</sub> : (m <sub>x</sub> , 0, m <sub>z</sub> ), (-m <sub>x</sub> , 0, -m <sub>z</sub> ), (-m <sub>x</sub> , 0, -m <sub>z</sub> ), (m <sub>x</sub> , 0, m <sub>z</sub> ) Pr <sub>2</sub> : (m <sub>x</sub> , 0, m <sub>z</sub> ), (-m <sub>x</sub> , 0, -m <sub>z</sub> ), (-m <sub>x</sub> , 0, -m <sub>z</sub> ), (m <sub>x</sub> , 0, m <sub>z</sub> )
	Pc2/c (13.74)	Pr <sub>1</sub> : (0, m <sub>y</sub> , 0), (0, m <sub>y</sub> , 0), (0, -m <sub>y</sub> , 0), (0, -m <sub>y</sub> , 0) Pr <sub>2</sub> : (0, m <sub>y</sub> , 0), (0, m <sub>y</sub> , 0), (0, -m <sub>y</sub> , 0), (0, -m <sub>y</sub> , 0)
	Pc2/c (13.74)	Pr <sub>1</sub> : (0, m <sub>y</sub> , 0), (0, -m <sub>y</sub> , 0), (0, -m <sub>y</sub> , 0), (0, m <sub>y</sub> , 0) Pr <sub>2</sub> : (0, m <sub>y</sub> , 0), (0, -m <sub>y</sub> , 0), (0, -m <sub>y</sub> , 0), (0, m <sub>y</sub> , 0)

<sup>a</sup> The atomic positions in fractional coordinate units [20] and the Wyckoff positions to the above magnetic order are:  
Pr1: 0.00000, 0.16590, 0.25000 - (0, y, 1/4), (0, -y, 3/4), (1/2, y+1/2, 1/4), (1/2, -y+1/2, 3/4)  
Pr2: 0.00000, 0.50100, 0.25000 - (0, y, 1/4), (0, -y, 3/4), (1/2, y+1/2, 1/4), (1/2, -y+1/2, 3/4)

try of the compound, the magnetic structures obtained for the propagation vector  $k_m = (0,0,0)$  are the same for  $k_m = (1,1,0)$ .

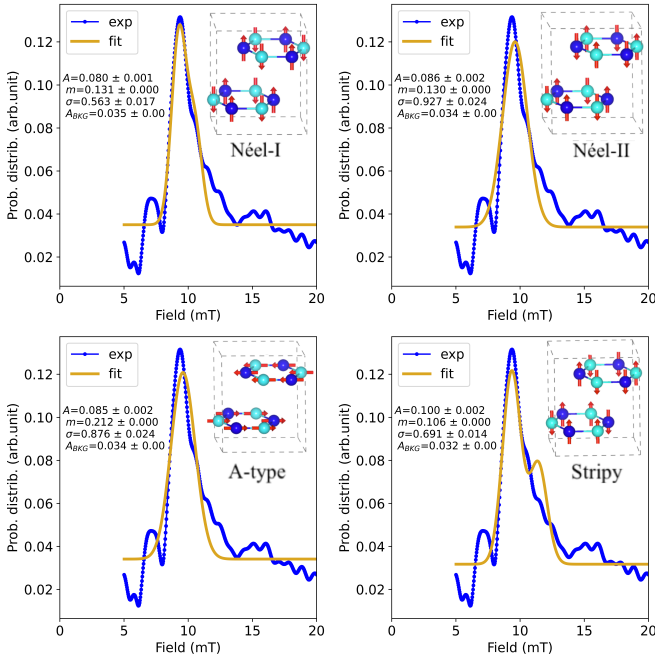


FIG. 6. Comparison between experimental and calculated dipolar field distribution for four candidate magnetic structures. Fit parameters from Eqs. A1-A3 are shown in the inset of each panel.

In order to obtain the magnetic structure and estimate the magnetic moment of Na<sub>2</sub>PrO<sub>3</sub> using the muon spin spectroscopy measurements, we approximated and fit the Gaussian convolution of the muon dipolar fields calculated over these 28 magnetic structures to the experimentally observed Fourier power spectrum at 1.5 K. The simulation of the dipolar contribution to the muon internal field also requires the knowledge of the muon site [43]. As described in the main text, the muon was found to thermalize at three symmetrically inequivalent sites, that we have labelled A<sub>1</sub>, A<sub>2</sub>, and A<sub>3</sub> (See Main text Sec. III A 1). Each of these sites has a multiplicity of 8 (8f Wyckoff position), hence we have considered dipolar fields calculated on 24 muon positions.

For each magnetic structure, the dipolar fields  $B$  [43] are calculated for all 24 muon sites with index  $i$ , in the pristine Na<sub>2</sub>PrO<sub>3</sub> structure as a function of the Pr moments,  $m_{Pr}$ , written as

$$p(B, m_{Pr}) = \sum_{i=1}^{24} \delta(B - m_{Pr} B_i). \quad (A1)$$

Such that we can approximate the FFT distribution of the ZF- $\mu$ SR experimental spectra to a convolution with a Gaussian broadening  $g$  as

$$\tilde{p}(B, m_{Pr}, \sigma) = (p * g)(B) := \int_{-\infty}^{\infty} p(\tau, m) g(B - \tau, \sigma) d\tau. \quad (A2)$$

The fitting function  $P$  becomes

$$P(B; m, \sigma, A, A_{BKG}) = A\tilde{p}(B, m, \sigma) + A_{BKG}, \quad (\text{A3})$$

where  $\sigma$ ,  $A$ ,  $A_{BKG}$  are the width, amplitude and the background of the distribution respectively. Statistically acceptable fits were obtained only for four magnetic configurations shown in Fig. 6. These magnetic structures consist of the Néel-I, Néel-II, A-type, and Stripy antiferromagnetic configurations.

- 
- [1] G. Jackeli and G. Khaliullin, Mott Insulators in the Strong Spin-Orbit Coupling Limit: From Heisenberg to a Quantum Compass and Kitaev Models, *Phys. Rev. Lett.* **102**, 017205 (2009).
- [2] H. Takagi, T. Takayama, G. Jackeli, G. Khaliullin, and S. E. Nagler, Concept and realization of Kitaev quantum spin liquids, *Nature Reviews Physics* **1**, 264 (2019).
- [3] Y. Motome, R. Sano, S. Jang, Y. Sugita, and Y. Kato, Materials design of Kitaev spin liquids beyond the Jackeli–Khaliullin mechanism, *Journal of Physics: Condensed Matter* **32**, 404001 (2020).
- [4] G. Khaliullin, Orbital Order and Fluctuations in Mott Insulators, *Progress of Theoretical Physics Supplement* **160**, 155 (2005), <https://academic.oup.com/ptps/article-pdf/doi/10.1143/PTPS.160.155/5162453/160-155.pdf>.
- [5] J. G. Rau, E. K.-H. Lee, and H.-Y. Kee, Generic Spin Model for the Honeycomb Iridates beyond the Kitaev Limit, *Phys. Rev. Lett.* **112**, 077204 (2014).
- [6] V. M. Katukuri, S. Nishimoto, V. Yushankhai, S.-L. Drechsler, and J. van den Brink, Kitaev interactions between  $j = 1/2$  moments in honeycomb  $\text{Na}_2\text{IrO}_3$  are large and ferromagnetic: insights from ab initio quantum chemistry calculations, *New Journal of Physics* **16**, 013056 (2016).
- [7] J. Chaloupka, G. Jackeli, and G. Khaliullin, Kitaev–Heisenberg Model on a Honeycomb Lattice: Possible Exotic Phases in Iridium Oxides  $\text{A}_2\text{IrO}_3$ , *Phys. Rev. Lett.* **105**, 027204 (2010).
- [8] Y. Singh, S. Manni, J. Reuther, T. Berlijn, R. Thomale, W. Ku, S. Trebst, and P. Gegenwart, Relevance of the Heisenberg–Kitaev Model for the Honeycomb Lattice Iridates  $\text{A}_2\text{IrO}_3$ , *Phys. Rev. Lett.* **108**, 127203 (2012).
- [9] R. D. Johnson, S. C. Williams, A. A. Haghhighrad, J. Singleton, V. Zapf, P. Manuel, I. I. Mazin, Y. Li, H. O. Jeschke, R. Valentí, and R. Coldea, Monoclinic crystal structure of  $\alpha$ - $\text{RuCl}_3$  and the zigzag antiferromagnetic ground state, *Phys. Rev. B* **92**, 235119 (2015).
- [10] J. A. Sears, L. E. Chern, S. Kim, P. J. Bercier, S. Francoual, Y. B. Kim, and Y.-J. Kim, Ferromagnetic Kitaev interaction and the origin of large magnetic anisotropy in  $\alpha$ - $\text{RuCl}_3$ , *Nature Physics* **16**, 837 (2020).
- [11] Y. Sugita, Y. Kato, and Y. Motome, Antiferromagnetic Kitaev interactions in polar spin-orbit Mott insulators, *Phys. Rev. B* **101**, 100410 (2020).
- [12] S. Trebst and C. Hickey, Kitaev materials, *Physics Reports* **950**, 1 (2022), kitaev materials.
- [13] K. W. Plumb, J. P. Clancy, L. J. Sandilands, V. V. Shankar, Y. F. Hu, K. S. Burch, H.-Y. Kee, and Y.-J. Kim,  $\alpha$ - $\text{RuCl}_3$ : A spin-orbit assisted Mott insulator on a honeycomb lattice, *Phys. Rev. B* **90**, 041112 (2014).
- [14] A. Banerjee, J. Yan, J. Knolle, C. A. Bridges, M. B. Stone, M. D. Lumsden, D. G. Mandrus, D. A. Tennant, R. Moessner, and S. E. Nagler, Neutron scattering in the proximate quantum spin liquid  $\alpha$ - $\text{RuCl}_3$ , *Science* **356**, 1055 (2017).
- [15] H. Liu and G. Khaliullin, Pseudospin exchange interactions in  $d^7$  cobalt compounds: Possible realization of the Kitaev model, *Phys. Rev. B* **97**, 014407 (2018).
- [16] R. Sano, Y. Kato, and Y. Motome, Kitaev–Heisenberg Hamiltonian for high-spin  $d^7$  Mott insulators, *Phys. Rev. B* **97**, 014408 (2018).
- [17] S.-H. Jang, R. Sano, Y. Kato, and Y. Motome, Antiferromagnetic Kitaev interaction in  $f$ -electron based honeycomb magnets, *Phys. Rev. B* **99**, 241106 (2019).
- [18] S.-H. Jang, R. Sano, Y. Kato, and Y. Motome, Computational design of  $f$ -electron Kitaev magnets: Honeycomb and hyperhoneycomb compounds  $\text{A}_2\text{PrO}_3$  ( $A = \text{alkali metals}$ ), *Phys. Rev. Mater.* **4**, 104420 (2020).
- [19] Y. Hinatsu and Y. Doi, Crystal structures and magnetic properties of alkali-metal lanthanide oxides  $\text{A}_2\text{LnO}_3$  ( $A = \text{Li, Na; Ln} = \text{Ce, Pr, Tb}$ ), *Journal of Alloys and Compounds* **418**, 155 (2006), proceedings of the Twenty-fourth Rare Earth Research Conference.
- [20] A. Ramanathan, J. E. Leisen, and H. S. La Pierre, In-Plane Cation Ordering and Sodium Displacements in Layered Honeycomb Oxides with Tetravalent Lanthanides:  $\text{Na}_2\text{LnO}_3$  ( $\text{Ln} = \text{Ce, Pr, and Tb}$ ), *Inorganic Chemistry* **60**, 1398 (2021).
- [21] M. J. Daum, A. Ramanathan, A. I. Kolesnikov, S. Calder, M. Mourigal, and H. S. La Pierre, Collective excitations in the tetravalent lanthanide honeycomb antiferromagnet  $\text{Na}_2\text{PrO}_3$ , *Phys. Rev. B* **103**, L121109 (2021).
- [22] A. Ramanathan, J. Kaplan, D.-C. Sergentu, J. A. Branson, M. Ozerov, A. I. Kolesnikov, S. G. Minasian, J. Autschbach, J. W. Freeland, Z. Jiang, M. Mourigal, and H. S. La Pierre, Chemical design of electronic and magnetic energy scales of tetravalent praseodymium materials, *Nature Communications* **14**, 3134 (2023).
- [23] A. Suter and B. Wojek, Musrfit: A Free Platform-Independent Framework for  $\mu\text{SR}$  Data Analysis, *Physics Procedia* **30**, 69 (2012), 12th International Conference on Muon Spin Rotation, Relaxation and Resonance ( $\mu\text{SR}2011$ ).
- [24] J. S. Möller, P. Bonfà, D. Ceresoli, F. Bernardini, S. J. Blundell, T. Lancaster, R. D. Renzi, N. Marzari, I. Watanabe, S. Sulaiman, and M. I. Mohamed-Ibrahim, Playing quantum hide-and-seek with the muon: localizing muon stopping sites, *Physica Scripta* **88**, 068510 (2013).
- [25] P. Bonfà and R. De Renzi, Toward the Computational Prediction of Muon Sites and Interaction Parameters, *Journal of the Physical Society of Japan* **85**, 091014 (2016).
- [26] I. J. Onuorah, P. Bonfà, and R. De Renzi, Muon contact hyperfine field in metals: A DFT calculation, *Phys. Rev. B* **97**, 174414 (2018).
- [27] S. J. Blundell and T. Lancaster, DFT+ $\mu$ : Density functional theory for muon site determination, *Applied Physics Reviews* **10** (2023).
- [28] J. P. Perdew, K. Burke, and M. Ernzerhof, Generalized Gradient Approximation Made Simple, *Phys. Rev. Lett.* **77**, 3865 (1996).
- [29] P. Giannozzi, S. Baroni, N. Bonini, M. Calandra, R. Car, C. Cavazzoni, D. Ceresoli, G. L. Chiarotti, M. Cococcioni, I. Dabo, A. Dal Corso, S. de Gironcoli, S. Fabris, G. Fratesi, R. Gebauer, U. Gerstmann, C. Gougoussis, A. Kokalj, M. Lazzeri, L. Martin-Samos, N. Marzari, F. Mauri, R. Maz-

- zarello, S. Paolini, A. Pasquarello, L. Paulatto, C. Sbraccia, S. Scandolo, G. Scauzero, A. P. Seitsonen, A. Smogunov, P. Umari, and R. M. Wentzcovitch, QUANTUM ESPRESSO: a modular and open-source software project for quantum simulations of materials, *Journal of Physics: Condensed Matter* **21**, 395502 (19pp) (2009).
- [30] P. E. Blöchl, Projector augmented-wave method, *Phys. Rev. B* **50**, 17953 (1994).
- [31] H. J. Monkhorst and J. D. Pack, Special points for Brillouin-zone integrations, *Phys. Rev. B* **13**, 5188 (1976).
- [32] G. E. Granroth, A. I. Kolesnikov, T. E. Sherline, J. P. Clancy, K. A. Ross, J. P. C. Ruff, B. D. Gaulin, and S. E. Nagler, SE-QUOIA: A newly operating chopper spectrometer at the SNS, *Journal of Physics: Conference Series* **251**, 012058 (2010).
- [33] S. J. Blundell, R. De Renzi, T. Lancaster, and F. L. Pratt, *Introduction to Muon Spectroscopy* (Oxford University Press, Oxford, 2022).
- [34] S. C. Cheung, Z. Guguchia, B. A. Frandsen, Z. Gong, K. Yamakawa, D. E. Almeida, I. J. Onuorah, P. Bonfá, E. Miranda, W. Wang, D. W. Tam, Y. Song, C. Cao, Y. Cai, A. M. Hallas, M. N. Wilson, T. J. S. Munsie, G. Luke, B. Chen, G. Dai, C. Jin, S. Guo, F. Ning, R. M. Fernandes, R. De Renzi, P. Dai, and Y. J. Uemura, Disentangling superconducting and magnetic orders in  $\text{NaFe}_{1-x}\text{Ni}_x\text{As}$  using muon spin rotation, *Phys. Rev. B* **97**, 224508 (2018).
- [35] L. Le, A. Keren, G. Luke, W. Wu, Y. Uemura, M. Tamura, M. Ishikawa, and M. Kinoshita, Searching for spontaneous magnetic order in an organic ferromagnet.  $\mu\text{SR}$  studies of  $\beta$ -phase p-NPNN, *Chemical Physics Letters* **206**, 405 (1993).
- [36] M. Campostrini, M. Hasenbusch, A. Pelissetto, P. Rossi, and E. Vicari, Critical exponents and equation of state of the three-dimensional Heisenberg universality class, *Phys. Rev. B* **65**, 144520 (2002).
- [37] F. L. Pratt, P. M. Zielinski, M. Bałanda, R. Podgajny, T. Wasutyński, and B. Sieklucka, A  $\mu\text{SR}$  study of magnetic ordering and metamagnetism in a bilayered molecular magnet, *Journal of Physics: Condensed Matter* **19**, 456208 (2007).
- [38] M. Smidman, D. T. Adroja, A. D. Hillier, L. C. Chapon, J. W. Taylor, V. K. Anand, R. P. Singh, M. R. Lees, E. A. Goremychkin, M. M. Koza, V. V. Krishnamurthy, D. M. Paul, and G. Balakrishnan, Neutron scattering and muon spin relaxation measurements of the noncentrosymmetric antiferromagnet  $\text{CeCoGe}_3$ , *Phys. Rev. B* **88**, 134416 (2013).
- [39] M. Majumder, R. S. Manna, G. Simutis, J. C. Orain, T. Dey, F. Freund, A. Jesche, R. Khasanov, P. K. Biswas, E. Bykova, N. Dubrovinskaia, L. S. Dubrovinsky, R. Yadav, L. Hozoi, S. Nishimoto, A. A. Tsirlin, and P. Gegenwart, Breakdown of Magnetic Order in the Pressurized Kitaev Iridate  $\beta\text{-Li}_2\text{IrO}_3$ , *Phys. Rev. Lett.* **120**, 237202 (2018).
- [40] T. Shiroka, G. Lamura, S. Sanna, G. Prando, R. De Renzi, M. Tropeano, M. R. Cimberle, A. Martinelli, C. Bernini, A. Palenzona, R. Fittipaldi, A. Vecchione, P. Carretta, A. S. Siri, C. Ferdeghini, and M. Putti, Long- to short-range magnetic order in fluorine-doped  $\text{CeFeAsO}$ , *Phys. Rev. B* **84**, 195123 (2011).
- [41] E. Holzschuh, A. B. Denison, W. Kündig, P. F. Meier, and B. D. Patterson, Muon-spin-rotation experiments in orthoferrites, *Phys. Rev. B* **27**, 5294 (1983).
- [42] J. Perez-Mato, S. Gallego, E. Tasci, L. Elcoro, G. de la Flor, and M. Aroyo, Symmetry-Based Computational Tools for Magnetic Crystallography, *Annual Review of Materials Research* **45**, 217 (2015).
- [43] P. Bonfá, I. J. Onuorah, and R. D. Renzi, Introduction and a Quick Look at MUESR, the Magnetic Structure and mUon Embedding Site Refinement Suite, in *Proceedings of the 14th International Conference on Muon Spin Rotation, Relaxation and Resonance ( $\mu\text{SR}2017$ )*, Vol. 21 (2018).
- [44] H. Lutz, W. Eckers, and H. Haeuseler, OH stretching frequencies of solid hydroxides and of free  $\text{OH}^-$  ions, *Journal of Molecular Structure* **80**, 221 (1982).
- [45] B. Winkler, A. Friedrich, D. J. Wilson, E. Haussühl, M. Krisch, A. Bosak, K. Refson, and V. Milman, Dispersion Relation of an OH-Stretching Vibration from Inelastic X-Ray Scattering, *Phys. Rev. Lett.* **101**, 065501 (2008).
- [46] A. Scheie, *PyCrystalField*: software for calculation, analysis and fitting of crystal electric field Hamiltonians, *Journal of Applied Crystallography* **54**, 356 (2021).
- [47] See Supplemental Material at [URL will be inserted by publisher]. The Supplemental Material includes Refs. [46].
- [48] V. M. Katukuri, S. Nishimoto, V. Yushankhai, A. Stoyanova, H. Kandpal, S. Choi, R. Coldea, I. Rousochatzakis, L. Hozoi, and J. Van Den Brink, Kitaev interactions between  $j = 1/2$  moments in honeycomb  $\text{Na}_2\text{IrO}_3$  are large and ferromagnetic: insights from ab initio quantum chemistry calculations, *New Journal of Physics* **16**, 013056 (2014).
- [49] J. G. Rau and M. J. P. Gingras, Frustration and anisotropic exchange in ytterbium magnets with edge-shared octahedra, *Phys. Rev. B* **98**, 054408 (2018).
- [50] P. A. Maksimov and A. L. Chernyshev, Rethinking  $\alpha\text{-RuCl}_3$ , *Phys. Rev. Res.* **2**, 033011 (2020).
- [51] J. G. Rau, P. A. McClarty, and R. Moessner, Pseudo-Goldstone Gaps and Order-by-Quantum Disorder in Frustrated Magnets, *Phys. Rev. Lett.* **121**, 237201 (2018).
- [52] P. A. McClarty, X.-Y. Dong, M. Gohlke, J. G. Rau, F. Pollmann, R. Moessner, and K. Penc, Topological magnons in Kitaev magnets at high fields, *Phys. Rev. B* **98**, 060404 (2018).
- [53] J. G. Rau, R. Moessner, and P. A. McClarty, Magnon interactions in the frustrated pyrochlore ferromagnet  $\text{Yb}_2\text{Ti}_2\text{O}_7$ , *Phys. Rev. B* **100**, 104423 (2019).
- [54] M. E. Zhitomirsky and A. L. Chernyshev, Colloquium: Spontaneous magnon decays, *Rev. Mod. Phys.* **85**, 219 (2013).
- [55] M. Mourigal, W. T. Fuhrman, A. L. Chernyshev, and M. E. Zhitomirsky, Dynamical structure factor of the triangular-lattice antiferromagnet, *Phys. Rev. B* **88**, 094407 (2013).
- [56] Z. Weihong, J. Oitmaa, and C. J. Hamer, Second-order spin-wave results for the quantum XXZ and XY models with anisotropy, *Phys. Rev. B* **44**, 11869 (1991).